Clemson University
TigerPrints

Publications | Mechanical Engineering

1-2017

Demisting using an Ultrasonic Standing Wave Field

T. M. Merrell
Clemson University

John Saylor
Clemson University, jsaylor@clemson.edu

Follow this and additional works at: https://tigerprints.clemson.edu/mecheng_pubs

 Part of the Mechanical Engineering Commons

Recommended Citation
Please use the publisher's recommended citation. http://asa.scitation.org/doi/10.1121/1.4973689

This Article is brought to you for free and open access by the Mechanical Engineering at TigerPrints. It has been accepted for inclusion in Publications by an authorized administrator of TigerPrints. For more information, please contact kokeefe@clemson.edu.

Demisting using an ultrasonic standing wave field

T. M. Merrell and J. R. Saylor[a)]
Department of Mechanical Engineering, Clemson University, Clemson, South Carolina 29634-0921, USA

(Received 11 April 2016; revised 15 December 2016; accepted 22 December 2016; published online 13 January 2017)

Removing drops from an air flow can be challenging, particularly, for small drops. Herein a method for demisting is presented that employs ultrasonics to force small drops to combine. Specifically, a cylindrical ultrasonic standing wave field is established in a tube, forming pressure nodes that take the form of cylinders located within the tube and having the same axis as the tube. Droplets are driven toward these pressure nodes by the acoustic radiation force, forcing smaller drops to combine to form larger drops, which eventually fall due to gravity, thereby demisting the flow. Experiments presented herein show that, for the setup employed, this method can remove a fraction of drops that approaches 0.8 and that the improvement due to ultrasonics, compared to the case without ultrasonics, is as large as 2.8. The effect of air flow rate and power is investigated. © *2017 Acoustical Society of America*. [http://dx.doi.org/10.1121/1.4973689]

[MRH] Pages: 172–182

I. INTRODUCTION

A. Motivation

Demisting, the removal of liquid drops from a gas flow, is critical to an array of industrial processes. Drift eliminators in cooling towers reduce the need for make up water by collecting drops before exiting the flow loop. These demisters also decrease the impact and adverse health effects that these drops can have if exhausted.[1–5] In the area of water resources, fog collectors are sometimes used to generate potable water in parts of the world where water resources are constrained and fog is common due to favorable atmospheric conditions.[6–12] Monoethanolamine (MEA) sprays are used for removing carbon dioxide (CO_2) in natural gas processing,[13] and there is the potential for recovering CO_2 from fossil fuel power plant exhaust using this approach as well.[14] After use, MEA drops can be lost in aerosol form, and current systems prove insufficient at their retention.[15–17]

The demisters used in the applications described above rely on drop inertia to remove mist. Hence, the utility of all of these approaches is limited for small drops. In some situations, the drop size distribution is of such a form that the majority of the liquid mass exists in drops having diameters large enough to be removed by inertial methods. However, in other situations this is not the case and mist removal may be ineffective or impossible. For example, fog drops are typically quite small, with most of the mass of the fog drops on the order of 30 μm or smaller.[18,19] While inertial methods have some effect in this range of diameters, they are of limited effectiveness. A method that is effective at removing drops in this range, while maintaining the ability to remove larger drops, would be useful for some demisting applications. Of course, many of the above methods could remove smaller diameters by adding more obstacles to the flow path. For example, in mist eliminators, reducing the area open to air flow would eliminate drops that are smaller than would otherwise be the case. However, such an approach would increase the flow resistance, increase the pressure drop, and thereby increase the operating cost due to increased blower power (or spoil the convective flow structure in the case of natural draft cooling towers). Taking the above into account, what is needed is a method that does not increase the pressure drop of a flow, is capable of removing small drops (on the order of fog drop diameters), yet retains the ability to remove large drops as well. Herein, this is attempted via the generation of an ultrasonic standing wave field in a relatively large diameter tube (order of 0.01 m), having limited flow resistance.

An ultrasonic standing wave field used for drop manipulation is typically created by separating an ultrasonic transducer and a reflector by an integer number of half-wavelengths in a fashion similar to that shown in Fig. 1, which follows the general design presented by Trinh.[20] When drops or particles are in the vicinity of the standing wave field, the acoustic radiation force pushes them to the pressure nodes, resulting in an increase in their number density in that region, potentially causing the drops to combine and become large enough to fall, thereby resulting in demisting. This approach was used by Ran *et al.*[21] and Ran and Saylor[22] to improve particle scavenging by drops. Specifically, both drops and particles were introduced into the region of the standing wave field. These particles and drops combined in the pressure nodes, forming larger, particle-laden drops that eventually became large enough to fall, removing particles in the process.

The transducer setup shown in Fig. 1 could be used for demisting, however, to maximize the number of drops removed, the time that the mist is in the vicinity of the standing wave field should be maximized. Of course, greater demisting can be achieved simply by increasing the power delivered to the transducer. However, ideally an ultrasonic demister would maximize the mass of liquid removed per watt of input power. Increasing the residence time for a given input power allows drops that have been brought close

[a)]Electronic mail: jsaylor@clemson.edu

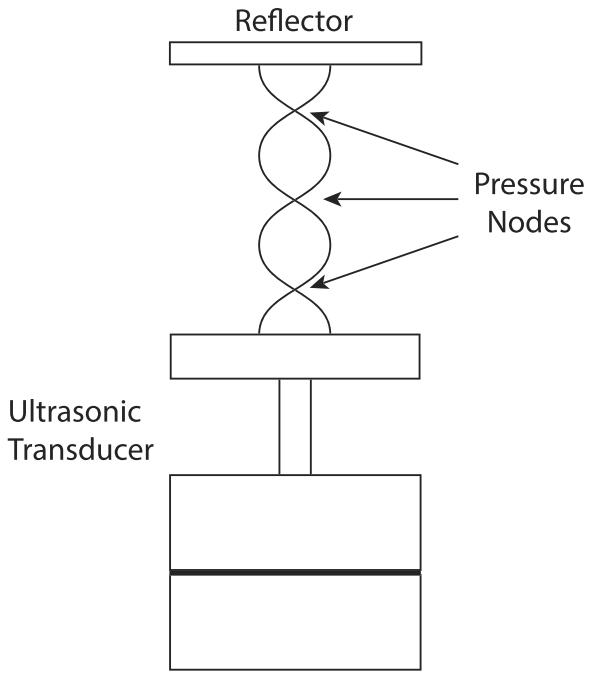

FIG. 1. Diagram of a typical disk-shaped faced ultrasonic transducer/reflector combination with accompanying standing wave field. When viewed down the axis, both transducer and reflector are circular in shape.

to each other in the pressure nodes adequate time to diffuse toward each other and to coalesce. To increase the residence time using the setup in Fig. 1 would require increasing the size of the disk-shaped ultrasonic transducers for a given flow speed. The commercial availability of such transducers effectively limits the size to the order of inches. To address this problem, we chose to create a tube that serves as a cylindrical ultrasonic resonator, creating pressure nodes that take the form of cylindrical shells having a length equal to that of the tube. Exploring the feasibility of such an approach is the goal of this work.

II. EXPERIMENTAL METHOD

The experimental setup used herein is presented in Fig. 2. The heart of the setup is the cylindrical resonator located in the sealing box. Figure 3 shows a detailed description of this resonator, which consisted of an aluminum tube with three bolt clamped Langevin transducers (SMBLTD45F28H, Steiner and Martins, Inc., Doral, FL) mounted on the tube midplane at 120° intervals around the tube circumference, enabling an axially symmetric forcing of the tube in its breathing mode. The Langevin transducers had a nominal natural frequency of 28 ± 1 kHz. When properly excited, a cylindrical ultrasonic standing wave field is established in the cylinder, causing mist to collect in the nodal rings of the standing wave field. Such nodal rings are shown in Fig. 3(b), where the view is down the axis of the tube. The Langevin transducers used here were chosen for convenience and cost. We note in passing that a cylindrical resonator can be created using a piezoelectric tube as was done by Kaduchak *et al.*[23] and Yang *et al.*[24] However, this approach is constrained by the length and diameter of piezoelectric tubes that are commercially available, which are limited to lengths of several inches. The method used here enables an essentially arbitrary

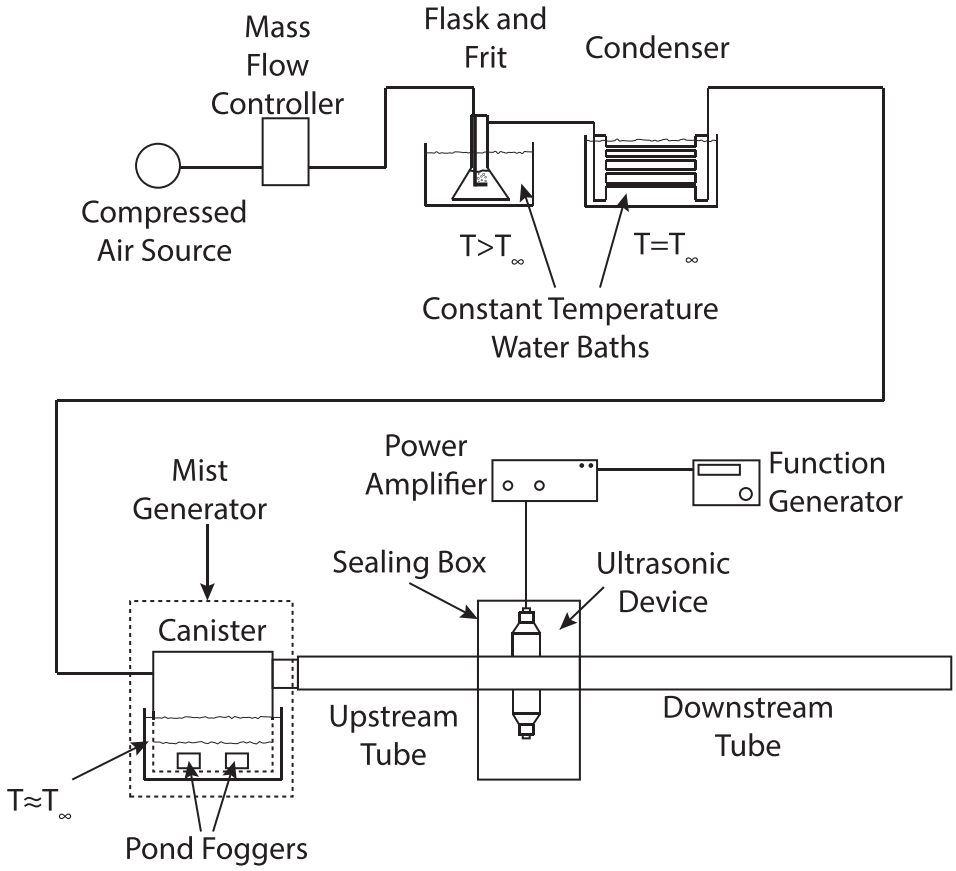

FIG. 2. Schematic of the experimental setup. Details of the ultrasonic resonator within the sealing box are presented in Fig. 3.

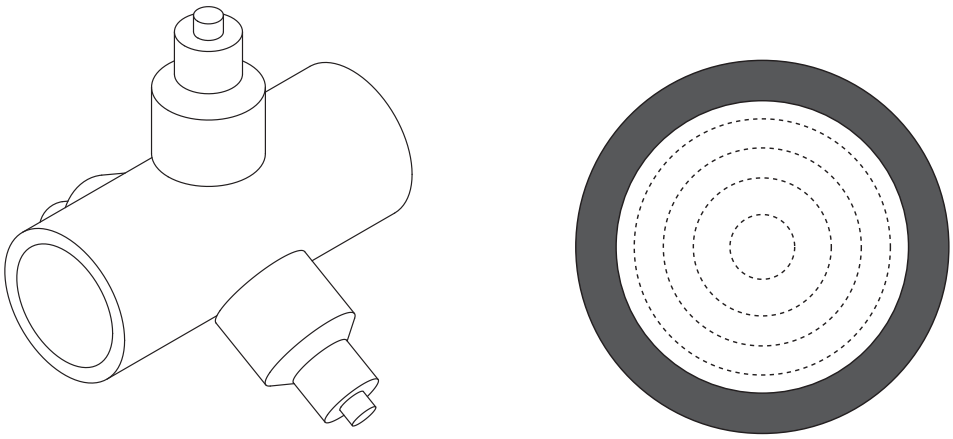

(a) (b)

FIG. 3. Schematic illustration of (a) the cylindrical resonator with three Langevin transducers mounted at the tube midplane, and (b) a depiction of the cylindrical pressure nodes, shown as dashed lines, as viewed down the axis of the cylindrical resonator. The cylindrical resonator had an inner diameter of 5.08 cm, an outer diameter of 6.35 cm, and a length of 12.7 cm.

tube length and diameter, although only a single tube length and diameter were explored herein.

Mist was generated via two pond foggers (F100, Alpine Corporation, Commerce, CA) inside an airtight canister. The pond foggers consist of ultrasonic transducers operating in the megahertz frequency range and create fine water mist at the water surface. The canister was filled with doubly distilled water, and in-house compressed air was used to convect the mist through the system. The flow rate was controlled by a mass flow controller (GFC47, Aalborg Instruments and Controls, Inc., Orangeburg, NY). The distribution of fog drop diameters was measured by coating a microscope slide with a thin film of paraffin oil and holding it perpendicular to the flow at the canister exit. Fog drops were allowed to deposit on the slide for about 10 s, after which time the slide was imaged by a microscope (Model DM750, Leica Microsystems Inc., Buffalo Grove, IL). Digital images of the deposited drops were acquired using a digital camera (Model EOS Rebel T3, Canon, U.S.A. Inc., Melville, NY), mounted on the microscope. A particle counting algorithm developed in ImageJ[25] was used to count the number and size of drops in each image. The optical system had a conversion factor of 0.05 μm/pixel, and the Abbe limit was 0.25 μm. Approximately 3–6 images were taken from a single slide, and about 40 images were used to produce a histogram. A drop size histogram was measured three times during the course of the experimental program to ensure it was not changing significantly. The average of these histograms is presented in Fig. 4, where D is the drop diameter. The median of this histogram was 5.4 μm and the root-mean-square (rms) was 2.0 μm. The average number density of mist drops flowing out of the canister was 7×10^5 drops/cm^3, which was obtained by dividing the volume rate of change of water in the canister by the product of the volume of a 5.4 μm drop and the volumetric flow rate of the air.

In order to minimize evaporative loss from the mist drops, the air was humidified by first bubbling it through a glass frit, which was submerged in water held at a temperature above room temperature (25 °C–32 °C). The air was then sent through a condenser consisting of a set of copper tubes immersed in a water bath held at room temperature, where excess water vapor was condensed out of the air flow. The humidity of the air leaving the condenser was measured before each run with a hygrometer (Digi-Sense HumidityLogR, Cole-Parmer Instrument Company, Vernon Hills, IL) to verify that the flow was near saturation; it was >98% for all runs.

The fog-laden flow exited the canister and then entered a system of three consecutive tubes as shown in Fig. 2. Upstream and downstream of the cylindrical resonator were two tubes referred to as passive tubes, as they are not directly driven by the Langevin transducers. These tubes were, however, acoustically excited by the cylindrical resonator and the mist flow revealed cylindrical pressure nodes in these tubes, as well as in the cylindrical resonator, which will be referred to as the "active tube" in contradistinction to the passive tubes. This is seen as an additional strength of this system—acoustic energy that would otherwise be dissipated into the environment is used to create pressure nodes within the passive tubes, causing additional demisting in these locations. The cylindrical resonator had an inner diameter of 5.08 cm, an outer diameter of 6.35 cm, and a length of 12.7 cm. The upstream and downstream passive tubes were made of clear acrylic, while the active tube was made of aluminum. Neither tubes were machined and were used as received from the manufacturer. Both passive tubes had an

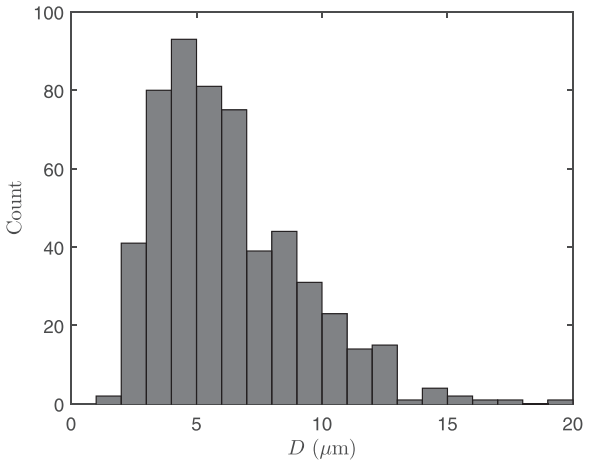

FIG. 4. Histogram of drop diameters, D. The width of each bin is 1 μm.

inner and outer diameter of 5.08 cm and 5.32 cm, respectively. The upstream and downstream passive tubes had lengths of 60 cm and 91.4 cm, respectively, while the resonator was 12.7 cm in length and had the same internal diameter as the passive tubes. It is noted that mist collection occurred primarily in the upstream and downstream tubes. This is because the intensity of the vibration of the wall of the active tube was sufficient to cause large drops to reatomize upon touching it. Hence, demisting appears to occur primarily by mist drop combinations that result in drops large enough to fall in the downstream tube and, to a lesser extent, in the upstream tube.

Directly connecting the passive tubes to the active tube was not possible, since such a connection would dampen the active tube and complicate the resonance of the system. To prevent this, a sealing box, indicated in Fig. 2, was created, which allowed a continuous flow between the tubes without a physical connection at the tube-to-tube interfaces. The box provided an air-tight seal with the two passive tubes, thereby preventing flow from leaking from the pipe into the atmosphere. There was a spacing between the active and passive tubes, which was <2 mm at both interfaces. During the experiments, no noticeable amount of mist was observed flowing into the box. Because of this, it is reasonable to believe that very few, if any, water drops were lost at these interfaces. As such, all the liquid drops must pass through the tubes, giving them opportunity to be removed. Were the sealing box not used, a significant fraction of drops may have exited through the interface and not passed through the entire setup, thus, affecting the total possible collection of mist.

The transducers were driven by the combination of a function generator (Model 33220A, Agilent Technologies, Santa Clara, CA) and power amplifier (model 7500, Krohn-Hite Corporation, Brockton, MA). The system had a very high Q-factor, and during the course of an experimental run the natural frequency would drift slightly, requiring a frequency tracking program to keep the system at resonance. This was done by monitoring the power delivered to the transducers and adjusting the frequency to keep the power at a maximum. The transducer current was obtained by measuring the voltage drop across a 1 Ω resistor in series with the resonator, and the voltage was measured across all three of the Langevin transducers. The voltages were sampled by an analog-to-digital (A/D) converter (Model DI-158U, Dataq Instruments, Inc., Akron, OH), and the rms power was computed as

$$P = vi\cos\phi, \tag{1}$$

where P is the power delivered to the transducer, v is the rms voltage across the transducers, i is the rms current through the transducers, and ϕ is the phase shift between the voltage and current. Although one would predict a maximum electrical power delivered to the transducers occurs for $\phi = 0°$, the largest P occurred for $\phi = 45°$, which preliminary experiments showed to also yield the strongest standing wave field, as evidenced by visualization of the pressure nodes via the mist. This is not surprising since the complicated coupling between the transducers, tube, and air cavity will not necessarily give maximum acoustic power at $\phi = 0°$. To automatically tune the system to maintain $\phi = 45°$, the voltage and current waveforms were sampled by the A/D converter which was controlled using the MATLAB programming environment (The Mathworks, Natick, MA). A sine wave was fit to both waveforms, ϕ was computed, and then f was updated to keep $\phi = 45°$. The system was able to update f at a rate of 4 times per second and ϕ was controlled to within $\pm 1°$.

The mist collection capability of the system presented in Fig. 2 is characterized by the mist collection efficiency, η, defined as

$$\eta = \frac{m_C}{m_L}, \tag{2}$$

where m_C and m_L are the mass of water collected in the system and the mass lost from the canister, respectively. A conservation of mass based method was used to obtain m_C and m_L. This was done by measuring the total mass of water having left the canister, and measuring the mass of mist that was collected. The total mass lost from the canister was found simply by weighing the canister before and after the experiment, the difference being m_L. The mass of collected water was found by weighing the upstream and downstream passive tubes before and after the experiment. For some of the parameter space tested, some water would accumulate on the active tube itself. In order to quantify this amount of water as well, a clean tissue was used to wipe up water that had collected on the active tube. The mass increase of the tissue was used to measure the mass deposited on the active tube wall. The mass of the canister and downstream tube was measured using a mechanical balance (Triple Pro 2610, Ohaus Corporation, Parsippany, NJ) with 0.1 g resolution. The upstream tube and tissue were measured on a digital scale (Model ZSA 210, Scientech Inc., Boulder, CO) with 0.001 g resolution. At higher power levels, and with sufficiently low air flow rates, the volume of water collected in the downstream tube was large enough to enable pouring it into a flask after which the water mass was then measured.

The length of each experiment was 8 min and each experiment yielded a single value for η. Experimental runs were conducted over a range of transducer powers and air flow rates. Ideally, the liquid flow rate also would have been varied independently, however, the amount of fog generated by the pond foggers was difficult to modulate. Also, these foggers did not always provide the same output. Accordingly, as will be discussed in Sec. III, the collection efficiency will be presented scaled to the concentration of water in the air C for each experiment (as well as in its raw form). This concentration is presented in units of mL of liquid water in the air per liter of air flow and was obtained by dividing the volumetric flow rate of water lost from the canister by the air volumetric flow rate. As will be shown below, scaling η to C accounts for variations in fog output.

III. RESULTS

The cylindrical resonator was driven nominally at a frequency of 28 kHz giving the $m = 4$ breathing mode. To

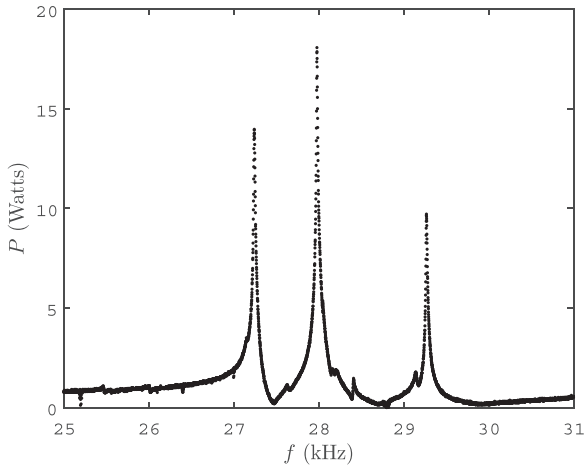

FIG. 5. Power P versus frequency f for the entire Langevin/tube setup shown in Fig. 3(a). The peaks occur at $f = 27.2$, 28, and 29.3 kHz.

characterize the resonance, the frequency was swept from 25 kHz to 31 kHz at a fixed voltage of $50V_{pp}$. Figure 5 is a plot of the resulting power delivered to the transducers P versus frequency. As the plot shows, three resonances are observed for the setup. One of these peaks exists at $f = 28$ kHz, which is within a few hundred Hz of the air cavity resonance predicted by

$$f = \frac{X_m c_0}{2\pi R_c} \tag{3}$$

for $m = 4$, where X_m is the mth zero of the Bessel function of the first kind, c_0 is the speed of sound in the cavity, and R_c is the radius of the cavity.[23] This is the largest peak in power consumption. However, the peak at 29.3 kHz was the frequency where the strongest cylindrical standing wave field was observed, as evidenced by the presence of nodal rings, visualized by the fine water mist itself, an example of which is shown in Fig. 6. The fact that the frequency at which the ultrasonic standing wave field is strongest is not the same as the frequency of the tallest peak in Fig. 5 is not necessarily surprising, since Fig. 5 is a plot of the power delivered to the transducers and not the acoustic power.

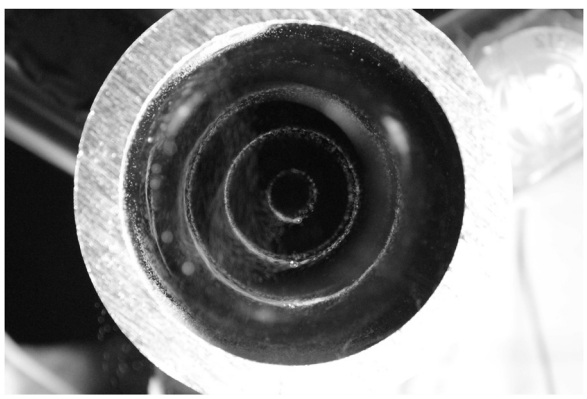

FIG. 6. Image of rings in the cylindrical ultrasonic standing wave field. The image is a view down the axis of the cylindrical resonator, and water mist is used to depict pressure node locations. Four nodes are present, although the outer fourth node is difficult to see. The driving frequency is 29.3 kHz.

The results of the experiments are now presented in the following plots, where each point is the average of the runs conducted for that location in the parameter space, and the vertical bars are 95% confidence intervals for each point. Although the number of experimental runs conducted varied slightly, for the overwhelming majority of cases, each point is an average of six experimental runs. Plots of η versus air flow rate, Q, are presented in Fig. 7 with and without ultrasonics. For the ultrasonics case, the transducer power was kept constant at $P = 6.63 \pm 0.24$ W. This value of P was chosen because it was intermediate between the largest and smallest powers explored when P was varied (see subsequent plots). As the flow rate is increased, η decreases. The plot shows that the presence of ultrasonics increases the collection efficiency of the mist drops at some flow rates by more than a factor of 2.

The decrease in collection efficiency η with air flow rate Q for the ultrasonics case presented in Fig. 7 is expected, since increasing Q means a lower residence time in the ultrasonic resonator (and passive tubes), and therefore less time for the ultrasonic standing wave field to act to combine mist drops, which would make them heavier and able to fall out of the flow. This explanation implicitly assumes that the concentration of mist drops is constant, since variation in the concentration of drops should also affect collection efficiency, viz., the higher the mist concentration, the easier it would be for drops to combine via ultrasonics and be eliminated. Regardless of the air flow rate, the mist generation setup was operated the same; the number of pond foggers was fixed, and the power delivered to them was fixed. Thus, the rate at which drops were formed should be the same, regardless of air flow rate Q. This might seem to suggest that the total mass of water and the total number of drops convected into the ultrasonic resonator was the same for all runs, a situation which would be problematic, since it would result in the drop concentration increasing with decreasing Q. However, this is not the case. Figure 8 (left axis) is a plot of water mass lost m_L versus Q, showing that the mass of water drops leaving the mist generation setup increases with Q for all of the flow rates tested herein. Essentially this means that the foggers are creating more drops than can be

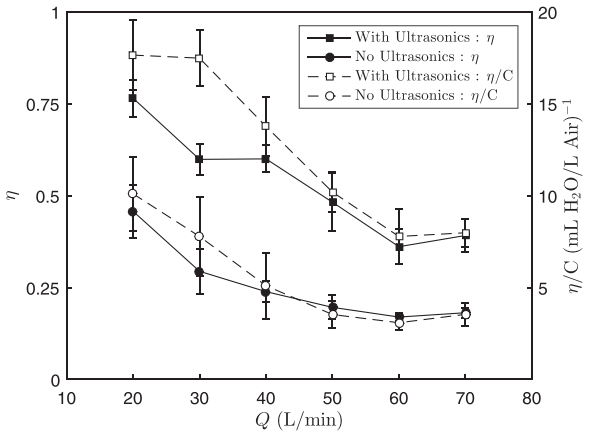

FIG. 7. Left axis: Collection efficiency η versus air flow rate Q, both with and without ultrasonics. Right axis: Collection efficiency scaled to water concentration C versus air flow rate. Electrical power delivered to the transducers was held constant at $P = 6.63 \pm 0.24$ W.

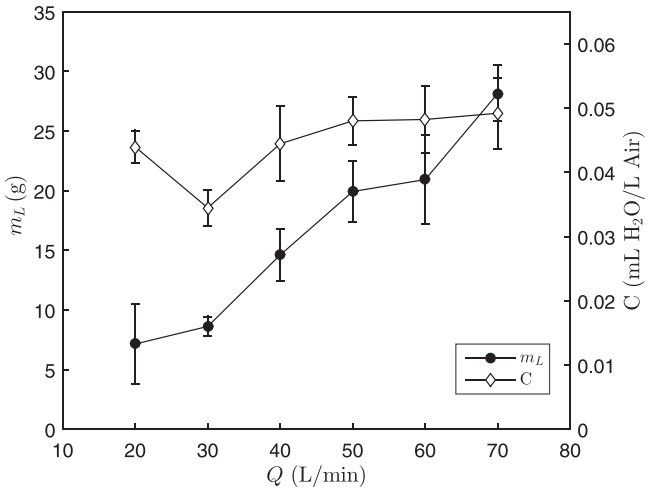

FIG. 8. Left axis: Mass lost m_L versus air flow rate Q. Right axis: Concentration of water in air C versus air flow rate Q. Vertical bars are 95% confidence intervals.

convected away and that some portion of the drops that are formed fall back into the water of the mist generation setup, indicating that the mist generator acts as a reservoir of water drops, providing more of them to the ultrasonic resonator as Q is increased. This is further illustrated on the right-hand axis of Fig. 8 where the concentration of water in air, C, in units of mL H_2O/L air is plotted against Q. Values of C are obtained by dividing the volumetric flow rate of water lost from the canister by the air volumetric flow rate. The plot of C versus Q in Fig. 8 shows that C is relatively constant, although there is variation around $Q = 30$ L/min. Note that C can also be thought of as the drop number concentration, at least until significant mist removal begins to occur. Hence, the change in collection efficiency with Q shown for the ultrasonics case in Fig. 7 is primarily due to residence time, since, as Fig. 8 shows, the drop concentration is essentially constant. However, since there is some variation in C with Q shown in Fig. 8 (right axis), the collection efficiency η is shown on the right axis of Fig. 7 as η/C versus Q. The η and η/C trends in Fig. 7 are not appreciably different, suggesting that the variation in C with Q in these experiments is not large enough to appreciably affect the trend in η. However, it is true that the η/C plot in Fig. 7 is smoother than η and it may be that the small variations shown in Fig. 8 serve primarily to add noise to the η results, which are eliminated when η/C is plotted.

The decrease in η with Q for the no-ultrasonics case in Fig. 7 is also due to a decreasing residence time. As will be demonstrated in Sec. IV, without ultrasonics drops are removed primarily by gravitational settling without combinations or collisions. The shorter the residence time, the less settling there will be, resulting in a decrease in η with Q.

The relative increase in η due to ultrasonics is quantified by the ratio

$$R = \frac{(\eta/C)_u}{(\eta/C)_{wo}}, \tag{4}$$

where $(\eta/C)_u$ is η/C with ultrasonics, and $(\eta/C)_{wo}$ is η/C without ultrasonics. R is plotted against Q in Fig. 9

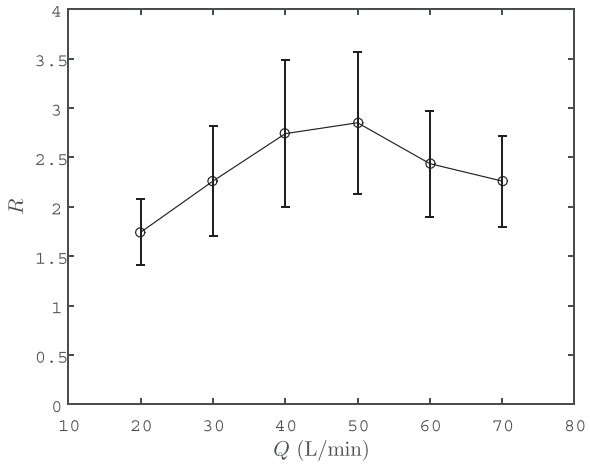

FIG. 9. Ratio of η/C with and without ultrasonics, R, versus air flow rate Q; $P = 6.63 \pm 0.24$ W.

showing that the improvement in mist removal ranges from 1.7 to 2.8 for the range of flow rates and mist concentration considered here. These averaged data suggest a maximum in R at intermediate Q, however, the confidence intervals are large, preventing a conclusion regarding an extremum.

To observe the effect of power on mist removal, the collection efficiency η and η/C are plotted against power P in Fig. 10. Here, the flow rate is held constant at $Q = 50 \pm 1$ L/min. This plot shows η increases with the power delivered to the transducers up until about 8 W, after which η remains effectively constant with further increases in power (within the 95% confidence intervals). The reason for this asymptote will be discussed in Sec. IV. The same basic trend is observed for η/C as for η in Fig. 10. As was the case when the data were plotted against Q, here, the η/C results are smoother, for the same reason as noted above, namely, that variations in C have an effect on η and these are corrected for when η is scaled to C. Figure 11 is a plot R versus P for the same conditions as in Fig. 10 and showing the same trend, indicating that the *improvement* in η due to ultrasonics increases with P, but also flattens out to an asymptote at high power.

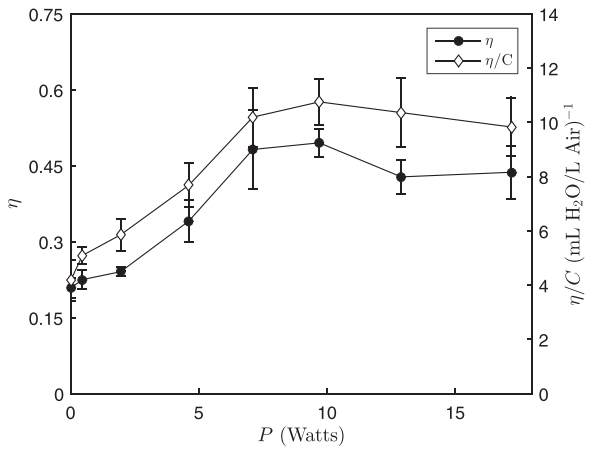

FIG. 10. Left axis: Collection efficiency η versus power P. Right axis: Ratio η/C versus power P. Flow rate of air is $Q = 50 \pm 1$ L/min.

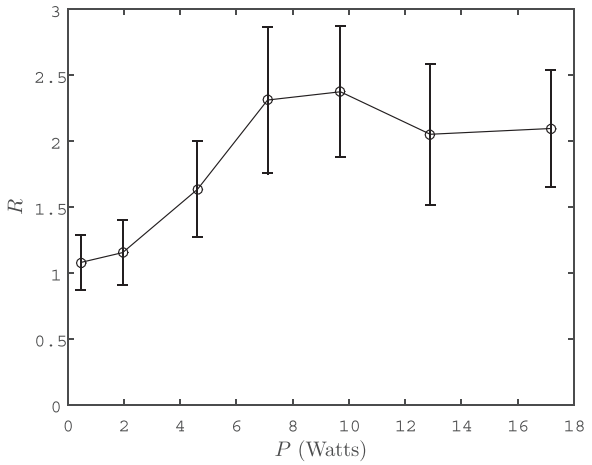

FIG. 11. R versus power P for $Q = 50 \pm 1$ L/min.

IV. DISCUSSION

The main results obtained from the experiments conducted herein are the following. First, the presence of ultrasonics enhances the removal of mist from a flow for the air flow rates, mist concentration, and transducer powers explored. The increase due to ultrasonics is as large as 2.8, as Fig. 9 shows, and η approaches 0.8 for the best case situation within the parameter space explored, as Fig. 7 shows. Second, the value of η and η/C decreases with flow rate for both the ultrasonics and no-ultrasonics cases. Finally, as the power delivered to the transducers increases, η/C increases up to a point, after which it flattens out. These results are further explored below and a possible mechanism explaining how ultrasonics enhances demisting is developed.

A. No-ultrasonics case

Although Figs. 7 and 9 reveal a significant increase in mist removal due to the ultrasonic standing wave field, it should be noted that without ultrasonics mist removal is still significant. For example, as Fig. 7 shows, at the lowest flow rate explored, η for the no-ultrasonics case is slightly less than 0.5, indicating that almost 50% of the mist is removed, even without ultrasonics. Because there is no ultrasonic field in this case, the only means for drop removal are impact with the tube walls due to some facet of the air flow, and/or gravitational settling. As is shown below, while some aspect of both are likely present, gravitational settling seems to explain most of the mist removal for this case.

Assuming Stokes flow and assuming that drops quickly attain terminal velocity, the settling velocity for the drops considered here can be described by[26]

$$S = \frac{(\rho_p - \rho_0)D^2 g}{18\mu_0}, \tag{5}$$

where ρ_p and ρ_0 are the drop and air densities, respectively, g is the gravitational acceleration, and μ_0 is the dynamic viscosity of air. The amount of mist collected was computed geometrically as the area overlap of two circles of identical size, one of which represents the falling mist, initially occupying the entire tube, and the other circle representing the unmoving tube. This is illustrated in Fig. 12 where the gray area represents the mist drops, which have fallen a sufficient distance to strike the tube wall in a period of time, t. The fraction of mist removed for this case is therefore related to the overlap area a of two circles of identical size

$$a = 2R_c^2 \cos^{-1}\left(\frac{l}{2R_c}\right) - \frac{l}{2}\sqrt{\left(4R_c^2 - l^2\right)}, \tag{6}$$

where l is the center-to-center distance between the two circles, and the radius of the circles is the radius of the tube, R_c. The resulting mist removal purely due to gravitational settling then is

$$\eta = 1 - \frac{a}{\pi R_c^2}. \tag{7}$$

Multiplying the settling velocity obtained from Eq. (5) by the residence time of the mist in the tube (which ranges from ~10 to 4 s for the 20–70 L/min flow rates investigated here), gives the center-to-center distance l, enabling computation of a and then η for the no-ultrasonics case from Eqs. (6) and (7), respectively. Figure 13 presents η predicted in this way, superimposed with the no-ultrasonics data from Fig. 7, plotted against Q. Figure 13 presents the behavior for the experimentally obtained drop diameter $D = 5.4\,\mu$m along with behavior obtained when D was iteratively adjusted to minimize the least squares difference between the experimental and predicted values of η, giving $D = 7.8\,\mu$m. The fact that D must be increased in order to get the data and settling model to match indicates that other mechanisms are helping remove mist beyond the gravitational settling. As noted above, this would be due to drop impaction with the tube walls due to some facet of the air flow. This could be due to, for example, fluctuations in the streamlines. The Reynolds number herein ranged from ~400 to 1500, thus, such non-laminar effects should be small. Nevertheless, if any water mass is lost due to inertial impaction, the iteratively obtained value of D will be larger in order for a purely gravitational settling explanation to work. Another possibility concerns the distribution of

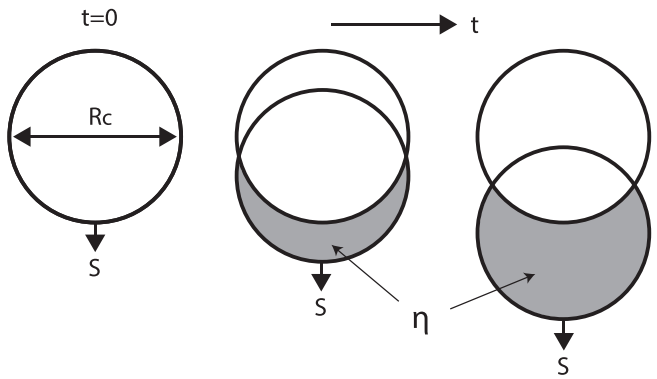

FIG. 12. Schematic illustration of fog settling onto tube walls for the no-ultrasonics case. The white circle on the left represents the tube with fog uniformly distributed throughout its cross section. The gray regions in the two subsequent diagrams represent the amount of fog that will have settled onto the tube wall in a time, t. The center-to-center distance between the two vertically displaced circles is l in Eq. (6).

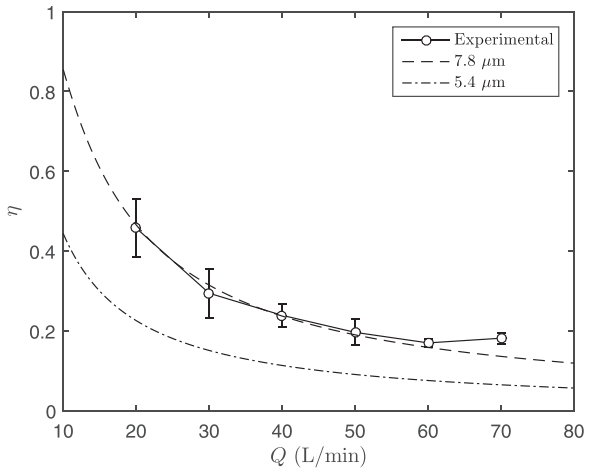

FIG. 13. Data without ultrasonics from Fig. 7, replotted with the settling theory for a drop diameter $D = 5.4\,\mu$m, as well as for $D = 7.8\,\mu$m, which was iteratively obtained to minimize the difference between the experimental and predicted values.

drop sizes. Although the drop diameter distribution is not extremely polydisperse, it does have an rms of 2.0 μm, and it is possible that drops of different diameters are combining as they settle, since they themselves have different settling velocities. This would, in turn, result in a larger effective average drop diameter, explaining the larger value of D obtained in fitting the data in Fig. 13.

B. Ultrasonics case

Even for the case of demisting in the presence of an ultrasonic standing wave field, drop removal is also ultimately due to gravitational settling, since some aspect of the ultrasonics results in an increase in drop diameter, resulting in removal via settling. The situation is more complicated, though, since the ultrasonic standing wave field supports drops at the nodal regions, holding them in place and preventing them from falling, to some degree. At the same time, in moving drops toward pressure nodes, the probability of drop collisions increases, promoting the formation of larger drops, which settle more rapidly once outside of the active tube and in the downstream passive tube where the field is weaker. Since η increases in the presence of ultrasonics, it must be the case that the effect of increasing the drop size is larger than the effect of the levitation capability.

Increasing the diameter of the drop has a significant effect on the settling velocity, since S increases as D^2 [Eq. (5)]. Assuming that the role of ultrasonics in enhancing mist collection is primarily due to making drops larger whereby they fall more rapidly, we posit the following three step process to explain the increase in η above that for the no-ultrasonics case. First, the acoustic radiation force brings drops closer together, increasing their number density above the value obtained at the canister exit (7×10^5 drops/cm^3). Second, thermal coagulation due to Brownian motion of the concentrated drops results in drop combinations, which increase the average drop diameter. Third, these large drops have a larger settling velocity and therefore are removed faster than would be the case without ultrasonics. To determine if this process can explain the experimental results, the equations for the acoustic radiation force and for thermal coagulation are presented and then applied to two sample experimental cases.

An equation for F_{ar} for the cylindrical setup shown in Fig. 3(a) has been developed by Barmatz *et al.*,[27]

$$F_{ar} = \frac{\tilde{F}\left(\pi D^3 \rho_0 U_0^2 k_\lambda\right)}{8}, \tag{8}$$

where

$$\tilde{F} = \left(\left[\left(\frac{2f_1}{3}\right) + \left(\frac{f_2}{2}\right)\right] J_0(\chi) - \left(\frac{f_2}{2}\right) J_2(\chi)\right) J_1(\chi), \tag{9}$$

$$f_1 = 1 - \frac{\rho_0 c_0^2}{\rho_p c_p^2}, \tag{10}$$

$$f_2 = \frac{2(\rho_p - \rho_0)}{2\rho_p + \rho_0}, \tag{11}$$

where J_n is the nth order Bessel function of the first kind, U_0 is the maximum acoustic velocity of fluid particles in the wave, k_λ is the acoustic wave number, c_p is the speed of sound in the drop, $\chi = k_\lambda r$ where r is the radial coordinate measured from the tube axis. Equation (8) is an inviscid form for F_{ar}. Such inviscid forms, for example, the seminal work due to King,[28] are valid for large drops. However, for small drops, viscous effects must be considered. Here, "large" means the drop is larger than the acoustic boundary layer thickness δ,

$$\delta = \sqrt{\frac{2\nu}{\omega}} \tag{12}$$

where ν is the kinematic viscosity of the air and ω is the angular frequency of the acoustic wave. At $f = 29$ kHz, the nominal frequency used in this work is $\delta = 14\,\mu$m. As this work concerns drop diameters smaller than this, a theory accounting for viscosity is needed. Such theories have been developed by Doinikov,[29–31] Danilov and Mironov,[32] and Settnes and Bruus;[33] however, none of these theories were developed specifically for the case of a cylindrical standing wave field. A modification to include viscosity for a plane wave is presented by Settnes and Bruus,[33] where Eq. (11) is replaced by

$$f_2(\tilde{\rho}_0, \tilde{\delta}) = \mathrm{Re}\left[\frac{2\left[1 - \gamma(\tilde{\delta})\right](\tilde{\rho}_0 - 1)}{2\tilde{\rho} + 1 - 3\gamma(\tilde{\delta})}\right], \tag{13}$$

where

$$\tilde{\rho} = \frac{\rho_p}{\rho_0}, \tag{14}$$

$$\gamma(\tilde{\delta}) = -(3/2)[1 + i(1 + \tilde{\delta})]\tilde{\delta} \tag{15}$$

and

$$\tilde{\delta} = \frac{\delta}{D/2}. \tag{16}$$

Applying this modification to Eq. (11), thus, leads to a viscous equation for the acoustic radiation force in the cylindrical standing wave field, which will be used below. We note in passing that recent work by Karlsen and Bruus[34] shows that the inclusion of thermoviscous effects in the development of F_{ar} can lead to very large differences from the viscous predictions developed above. According to that work, thermoviscous effects should not result in values of F_{ar} that deviate significantly from the viscous predictions presented here for the values of $\tilde{\delta}$ explored here. However, it is noted that decreasing the mist drop diameter by a factor of 10 or larger would cause thermoviscous effects to become significant.

Using Eqs. (8)–(10) and (12)–(16), an estimate can be obtained for the radial distance drops travel due to F_{ar}. An increase in the drop number density due to the acoustic radiation force can be obtained by integrating $F_{ar} - F_d$ over the active tube residence time, where F_d is the Stokes drag

$$F_d = 3\pi\mu_0 u_r D, \tag{17}$$

and u_r is the velocity of the drop in the radial direction. To do this, a value of U_0 is needed in Eq. (8), which was obtained by levitating a drop having a diameter on the order of a millimeter in our apparatus. By slowly reducing the power until the drop fell, which occurred at $P \sim 1$ W, and then setting the drop weight equal to F_{ar} gave $U_0 = 10$ m/s. Using this value for U_0, $F_{ar} - F_d$ was numerically integrated to find the distance traveled by a drop during the residence time in the ultrasonic standing wave field, assuming that F_{ar} scales linearly with P.

In this discussion, two experimental points will be considered from the plot of η versus P presented in Fig. 10: $P = 1.95$ W and $P = 9.70$ W. These points were chosen simply because they were closest to 1 and 10 W. The experimental values for η for these two cases is 0.241 and 0.495, respectively. These two values exceed the no-ultrasonics case in this plot ($P = 0$ W) by 0.03 and 0.286, respectively. For the $P = 1.95$ W case, $F_{ar} - F_d$ was integrated for the duration of the active tube residence time. The initial locations of the drops were assumed to all be at the antinodes, which gives a lower bound on the increase in the drop number density. This process gave an increase in the drop number density of 13.9, giving $N_0 = 9.7 \times 10^6$ drops/cm^3. Repeating this process for $P = 9.7$ W gives a factor of 6440 increase in number density, giving $N_0 = 4.51 \times 10^9$ drops/cm^3.

Once N_0 has been increased by F_{ar} as described above, the next step in the posited model is the combination of mist drops into larger mist drops due to thermal coagulation, which is the process whereby Brownian motion of drops causes collisions. The reduction in drop number density due to coagulation can be estimated as[26]

$$N(t) = \frac{N_0}{1 + N_0 K t} \tag{18}$$

where $N(t)$ is the number density at time, t, N_0 is the initial number density, and K is the coagulation coefficient. The coagulation coefficient for 5 μm drops is $K = 3.25 \times 10^{-10}$ cm^3/s.[26] For these conditions and the residence time for the results presented in Fig. 10, the increased value of N_0 caused by F_{ar} described above is reduced by thermal coagulation for $P = 1.95$ W and $P = 9.70$ W to $N/N_0 = 0.988$ and $N/N_0 = 0.146$, respectively. This reduction in number density results in an increase in the diameter of the drops that have combined. This increase is from the initial value of 5.4 μm to $D = 5.42$ μm at $P = 1.95$ W, and $D = 10.3$ μm at $P = 9.7$ W. Using these values in Eqs. (6) and (7) to obtain droplet removal due to gravitational settling of these now larger drops, again for the conditions of Fig. 10, gives an increase in η above that for the no-ultrasonics cases of 0.086 and 0.306, respectively. For the experimentally obtained data at these two values of P, the increase in η above that for the no-ultrasonics case is 0.03 and 0.286, respectively. The experimental and model results agree within an order of magnitude. It is noted that the modeled increase in drop number density due to the acoustic radiation force represents a very conservative case, as it only considers drop collisions once they are concentrated at the pressure node after having moved from an antinode. In actuality, many drops will have locations close to the node as they enter the system and, hence, the actual increase in drop number density will be higher, resulting in more drop combinations and a larger resulting drop diameter, which would bring the modeled and experimental results closer together at the lower power, although not at the higher power. While many assumptions are involved in the above analysis, the modeled process does predict the increase in η due to ultrasonics within 1 order of magnitude.

Another facet of the results that needs explanation is the asymptote in the η versus P plot in Fig. 10, which occurs at $P \sim 9$ W. It is noted that for the $P = 9.70$ W case, the increase in drop number density computed above gives $N_0 = 4.51 \times 10^9$ drops/cm^3. At this number density, the average center-to-center drop spacing is 6 μm, which is very close to where these 5.4 μm diameter drops would touch with even the most minimal thermal coagulation. Hence, it makes sense that further increases in P would not result in further increases in η since, after touching, the effective spacing between drops would become large, resulting in little subsequent increases in combinations and therefore little subsequent increases in η with power.

There are also several other mechanisms that could explain the increase in collection efficiency in the presence of an ultrasonic standing wave field. One of these is acoustic agglomeration, which is the combination of drops due to relative motion between drops of different size during the course of the period of the ultrasonic wave.[35] A parameter used to quantify acoustic agglomeration is the entrainment function H:[36]

$$H = \frac{u_p}{u_0} = \mathrm{Re}\left(\frac{1}{1 - i\omega\tau_d}\right), \tag{19}$$

where u_p and u_0 are the particle and fluid velocity, respectively, and τ_d is the particle relaxation time

$$\tau_d = \frac{1}{18}\frac{\rho_p D^2}{\mu_0}. \quad (20)$$

Essentially H is a measure of how closely drops in a standing wave field move to each other in the compression/rarefaction wave of the surrounding air. Relative motion between drops may occur if drops of different diameter are close to each other, each having a different value of u_p. Evaluating Eqs. (19) and (20) at $f = 29.3$ kHz, and $D = 3\,\mu$m and $D = 7\,\mu$m (a two rms bound around the average drop diameter) gives $H = 0.042$ and $H = 0.0015$, respectively. Using the maximum acoustic fluid velocity 10 m/s obtained previously for $P = 1$ W, and integrating a sinusoidal displacement of this magnitude gives a max fluid displacement of 110 μm, which gives maximum droplet displacements in one cycle of 4.62 μm and 0.165 μm for $D = 3\,\mu$m and 7 μm, respectively. This would require drops to be within a few microns of each other for this effect to play a role. Hence, acoustic agglomeration probably does occur and contribute to mist removal as F_{ar} increases the drop number density, but only at the highest of drop concentrations. As noted in the previous paragraph, this could be the case above $P \sim 9$ W in this work.

Relative motion can also occur on a different scale, as drops of different diameters are driven to the pressure nodes at different rates. This difference arises from the nonlinear relationship between F_{ar} and D for the viscid model. Evaluating this would require a complicated simulation of the three-dimensional trajectory of the drops as they move toward the nodes. It may be the case that this is also playing a role in the results seen herein, although it would probably have greatest impact as the particles get closer to the node, where their number densities are large.

Overall, the work presented herein shows that demisting can be achieved via the use of ultrasonic standing wave fields. In these laboratory experiments, as much as 80% of the fog whose diameters are on the order of 5 μm is removed using a power of less than 10 W. As noted in the Introduction, typical demisters force a drop-laden flow through a structure, which requires the flow to change direction whereupon drop inertia causes the drop to impact the structure, thereby removing it. For this approach to work for drops as small as those considered here is not impossible, it would simply require more blower power. Of course, power is needed to run the ultrasonics in the method investigated here. It is possible that the power required in the use of ultrasonics on an industrial scale would exceed the extra blower power that would be needed to remove the smaller drops using higher resistance demisters. However, this being the first study of demisting using ultrasonics, such engineering considerations are left as future work.

V. CONCLUSION

To the authors' knowledge, this is the first use of a cylindrical standing wave field for demisting. The cylindrical ultrasonic resonator used here was able to remove nearly 80% of the fog drops, by mass, at the lowest flow rate explored here. It is hypothesized that the movement of drops to the pressure nodes, by way of the acoustic radiation force, decreases the spacing between drops sufficiently that their diffusive motion leads to drop combinations and subsequent gravitational settling. Other mechanisms may be at play in parallel, also serving to demist the flow.

ACKNOWLEDGMENT

This work was funded by the National Science Foundation through Grant No. CBET-1336632.

[1]B. R. Becker and L. F. Burdick, "Effect of drift eliminator design on cooling tower performance," ASME J. Eng. Gas Turbines Power **114**, 632–642 (1992).
[2]T. J. Feeley, T. J. Skone, G. J. Stiegel, A. McNemar, M. Nemeth, B. Schimmoller, J. T. Murphy, and L. Manfredo, "Water: A critical resource in the thermoelectric power industry," Energy **33**(1), 1–11 (2008).
[3]H. Li, M. Hsieh, S. Chien, J. D. Monnell, D. A. Dzombak, and R. D. Vidic, "Control of mineral scale deposition in cooling systems using secondary-treated municipal wastewater," Water Res. **45**(2), 748–760 (2011).
[4]W. A. Hall, "Elimination of cooling tower fog from a highway," J. Air Pollut. Control Assoc. **12**(8), 379–383 (1962).
[5]H. T. El-Dessouky, I. M. Alatiqi, H. M. Ettouney, and N. S. Al-Deffeeri, "Performance of wire mesh mist eliminator," Chem. Eng. Process.: Process Intensif. **39**(2), 129–139 (2000).
[6]R. S. Schemenauer and P. Joe, "The collection efficiency of a massive fog collector," Atmos. Res. **24**, 53–69 (1989).
[7]R. S. Schemenauer and P. Cereceda, "A proposed standard fog collector for use in high-elevation regions," J. Appl. Meteorol. **33**, 1313–1322 (1994).
[8]R. S. Schemenauer and P. Cereceda, "Fog collection's role in water planning for developing countries," Nat. Resour. Forum **18**, 91–100 (1994).
[9]O. Klemm, R. S. Schemenauer, A. Lummerich, P. Cereceda, V. Marzol, D. Corell, J. van Heerden, D. Reinhard, T. Gherezqhiher, J. Olivier, P. Osses, J. Sarsour, E. Frost, M. J. Estrela, J. A. Valiente, and G. M. Fessehaye, "Fog as a fresh-water resource: Overview and perspectives," Ambio **41**, 221–234 (2012).
[10]C. M. Escobar, A. Lopez, H. F. Aristizabal, and J. M. Molina, "Operational fog collection and its role in environmental education and social reintegration: A case study in Columbia," in *Proceedings of the 5th International Conference on Fog, Fog Collection, and Dew* (2010), p. 133.
[11]J. Olivier and H. Rautenbach, "The implementation of fog water collection system in South Africa," Atmos. Res. **64**, 227–238 (2002).
[12]S. A. Abdul-Wahab, H. Al-Hinai, K. A. Al-Najar, and M. S. Al-Kalbani, "Feasibility of fog-water collection: A case study from Oman," J. Water Supply: Res. Technol.—AQUA **56**, 275–280 (2007).
[13]A. Rao and E. S. Rubin, "A technical, economic, and environmental assessment of amine-based CO_2 capture technology for power plant greenhouse gas control," Environ. Sci. Technol. **36**, 4467–4475 (2002).
[14]J. Mertens, H. Lepaumier, D. Desagher, and M. Thielens, "Understanding ethanolamine (MEA) and ammonia emissions from amine based post combustion carbon capture: Lessons learned from field tests," Int. J. Greenhouse Gas Control **13**, 72–77 (2013).
[15]G. T. Rochelle, "Amine scrubbing for CO_2 capture," Science **325**(5948), 1652–1654 (2009).
[16]J. Mertens, L. Brachert, D. Desagher, B. Schallert, P. Khakharia, and E. Goetheer, "Predicting amine mist formation based on aerosol number concentration and size measurements in flue gas," Energy Procedia **63**, 893–901 (2014).
[17]S. D. Sharma and M. Azzi, "A critical review of existing strategies for emission control in the monoethanolamine-based carbon capture process and some recommendations for improved strategies," Fuel **121**, 178–188 (2014).
[18]A. C. Best, "Drop-size distribution in cloud and fog," Q. J. R. Meteorol. Soc. **77**(333), 418–426 (1951).
[19]J. Podzimek, "Droplet concentration and size distribution in haze and fog," Stud. Geophys. Geod. **41**(3), 277–296 (1997).
[20]E. H. Trinh, "Compact acoustic levitation device for studies in fluid dynamics and material science in the laboratory and microgravity," Rev. Sci. Instrum. **56**, 2059–2065 (1985).

[21]W. Ran, J. R. Saylor, and R. G. Holt, "Improved particle scavenging by a combination of ultrasonics and water sprays," J. Aerosol Sci. **67**, 104–118 (2014).
[22]W. Ran and J. R. Saylor, "A mechanistic explanation of the increase in particle scavenging in the ultrasonic scrubber," J. Aerosol Sci. **87**, 88–101 (2015).
[23]G. Kaduchak, D. N. Sinha, and D. C. Lizon, "Novel cylindrical air-coupled acoustic levitation/concentration devices," Rev. Sci. Instrum. **73**, 1332–1336 (2002).
[24]J. Yang, H. Hwang, B. Youngmin, K. Moojoon, and H. Kanglyeol, "Trapping of microparticles in the cylindrical standing wave field," Proc. Symp. Ultrason. Electron. **33**, 281–282 (2012).
[25]W. S. Rasband, *ImageJ* (National Institutes of Health, Bethesda, MD, 1997–2009).
[26]W. C. Hinds, *Aerosol Technology: Properties, Behavior, and Measurement of Airborne Particles* (Wiley-Interscience, New York, 1982).
[27]M. Barmatz and P. Collas, "Acoustic radiation potential on a sphere in plane, cylindrical, and spherical standing wave fields," J. Acoust. Soc. Am. **77**, 928–945 (1985).
[28]L. V. King, "On the acoustic radiation pressure on spheres," Proc. R. Soc. London, Ser. A **147**(861), 212–240 (1934).
[29]A. A. Doinikov, "Acoustic radiation force on a spherical particle in a viscous heat-conducting fluid. I. General formula," J. Acoust. Soc. Am. **101**, 713–721 (1997).
[30]A. A. Doinikov, "Acoustic radiation force on a spherical particle in a viscous heat-conducting fluid. II. Force on a rigid sphere," J. Acoust. Soc. Am. **101**, 722–730 (1997).
[31]A. A. Doinikov, "Acoustic radiation force on a spherical particle in a viscous heat-conducting fluid. III. Force on a liquid drop," J. Acoust. Soc. Am. **101**, 731–740 (1997).
[32]S. D. Danilov and M. A. Mironov, "Mean force on a small sphere in a sound field in a viscous fluid," J. Acoust. Soc. Am. **107**, 143–153 (2000).
[33]M. Settnes and H. Bruus, "Forces acting on a small particle in an acoustical field in a viscous fluid," Phys. Rev. E **85**(1), 016327 (2012).
[34]J. T. Karlsen and H. Bruus, "Forces acting on a small particle in an acoustical field in a thermoviscous fluid," Phys. Rev. E **92**, 043010 (2015).
[35]J. A. Gallego-Juarez, E. Riera-Franco De Sarabia, G. Rodriguez-Corral, T. Hoffman, J. C. Galvez-Moraleda, J. J. Rodriguez-Maroto, F. J. Gomez-Morento, A. Bahillo-Ruiz, and M. Martin-Espigares, "Application of acoustic agglomeration to reduce fine particle emissions from coal combustion plants," Environ. Sci. Technol. **33**, 3843–3849 (1999).
[36]T. L. Hoffmann and G. H. Koopmann, "Visualization of acoustic particle interaction and agglomeration: Theory and experiments," J. Acoust. Soc. Am. **99**(4), 2130–2141 (1996).